ARTICLE

Membrane bending energy and tension govern mitochondrial division

Dora Mahecic[1,2*], Lina Carlini[1,2*], Tatjana Kleele[1,2], Adai Colom[2,3], Antoine Goujon[2,4], Stefan Matile[2,4], Aurélien Roux[2,3], and Suliana Manley[1,2]

[1] Institute of Physics, École Polytechnique Fédérale de Lausanne (EPFL), Route Cantonale, 1015 Lausanne, Switzerland

[2] National Centre for Competence in Research Programme Chemical Biology, Switzerland

[3] Department of Biochemistry, University of Geneva, CH-1211 Geneva, Switzerland

[4] Department of Organic Chemistry, University of Geneva, CH-1211 Geneva, Switzerland

[*] These authors contributed equally to this work

Correspondence should be addressed to

S.M. (email: suliana.manley@epfl.ch)

Abstract

Many molecular factors required for mitochondrial division have been identified; however, how they combine to physically trigger division remains unknown. Here, we report that constriction by the division machinery does not ensure mitochondria will divide. Instead, potential division sites accumulate molecular components and can constrict before either dividing, or relaxing back to an unconstricted state. Using time-lapse structured illumination microscopy (SIM), we find that constriction sites with higher local curvatures – reflecting an increased membrane bending energy – are more likely to divide. Furthermore, analyses of mitochondrial motion and shape changes demonstrate that dividing mitochondria are typically under an externally induced membrane tension. This is corroborated by measurements using a newly synthesized fluorescent mitochondrial membrane tension sensor, which reveal that depolymerizing the microtubule network diminishes mitochondrial membrane tension. We find that under reduced tension, the number of constrictions is maintained, but the probability that constrictions will divide is concomitantly reduced. These measurements allow us to establish a physical model, based on *in situ* estimates of membrane bending energy and tension, which accounts for the observed fates of mitochondrial constriction events.

Keywords: mitochondrial dynamics, mitochondrial division, membrane energetics

Introduction

Mitochondria are highly dynamic organelles, transported through the cytoplasm along cytoskeletal networks as they change in size and shape from long filaments to short fragments. Underlying such morphological changes are altered equilibria between fusion and division [1, 2]. These transformations have been linked to an adaptive response to cellular energy requirements,

for example in response to stress [3-5] or the cell cycle [6]. As a vestige of their bacterial origins, mitochondria cannot be generated *de novo*, but instead must multiply by division, or fission, of existing mitochondria [2]. Division has also been suggested to act as part of a quality control mechanism and an intracellular signal for mitophagy [7, 8].

In cellular division systems, internal assembly of the division machinery is tightly regulated and a series of cell cycle checkpoints ensure daughter cell viability. In contrast, the mitochondrial division machinery has been largely outsourced to the eukaryotic host cell and assembles on the outer surface of the organelle. Initially, the division site is marked by a pre-constriction defined by contact with ER tubules [9] and deformed by targeted actin polymerization [10-12]. Subsequently surface receptors including MiD49/51 [13], Mff [14, 15] and Fis1 [16] accumulate at the preconstriction and recruit dynamin related protein (Drp1) [17, 18]. Drp1 then oligomerizes into helices that wrap around mitochondria and hydrolyze GTP to provide a mechano-chemical force for constriction [19-21]. The dynamin 2 protein (Dyn2) is also reported to play a role downstream of Drp1 [22, 23].

This sequence of events leading to mitochondrial division, while frequently observed, is reported to be variable. For instance, the existence of multiple Drp1 adaptor proteins is indicative of their complementary roles [24], while Dyn2 has been shown to be a frequent, but non-essential partner in mediating mitochondrial fission [23], suggesting that different combinations of molecular machinery can lead to fission. Furthermore, deformations induced by external mechanical forces can trigger recruitment of the downstream machinery for mitochondrial fission [25]. These observations are consistent with the nature of membrane fission processes as requiring membrane deformation, agnostic of its origins. However, it remains unknown how mitochondria integrate the

forces imposed by the cytoplasmic machinery to regulate division. This is in part because it is challenging to quantify the effects of forces acting upon mitochondria in living cells.

To address these points, in this work we characterize the energies and forces required for mitochondrial division. Using time-lapse super-resolution imaging, we measure dynamic changes in membrane shape down to ~100 nm, in living cells. We observe that the presence of the fission machinery at mitochondrial constriction sites does not ensure division. We reveal that constrictions with higher bending energy are more likely divide, but leave a residual energy barrier to overcome. We find that constrictions were more likely to result in division when mitochondria were under higher membrane tension. A novel Fluorescence Lifetime Imaging (FLIM) mitochondrial membrane tension sensor demonstrated that mitochondrial membrane tension was reduced following perturbations to the microtubule network, a condition that resulted in fewer divisions and a higher frequency of reversals. Finally, using our *in situ* measurements, we established a physical model for mitochondrial division, in which elastic energy and membrane tension govern the kinetics and probability of fission.

Results

Constricted mitochondria frequently reverse to an unconstricted state

We performed live-cell SIM imaging of COS-7 cells transiently transfected with a mitochondrial matrix-localized GFP (mito-GFP) and Drp1-mCherry. We observed that highly constricted sites were typically marked by Drp1-mCherry, but while some proceeded to fission (Fig. 1a, Movie S1), others lost enrichment of Drp1 and relaxed to an unconstricted state (‘reversal’) (Fig. 1b, Movie S2). For quantification purposes, we defined ‘reversals’ as instances when a mitochondrion accumulated Drp1 at its constriction site and reached a diameter below 200 nm before relaxing

(Fig. 1c, d). Overall, 66% of constriction sites with Drp1 proceeded to fission (N=112, Fig. 1a, SFig. 1a-d), while the remaining 34% relaxed to an unconstricted state (N=57, Fig. 1b, SFig. 1e-h). Similar "reversible" or "non-productive" Drp1 constrictions were previously reported in yeast [26] and mammalian cells [12]. However, the features that distinguish reversals from fissions were not investigated.

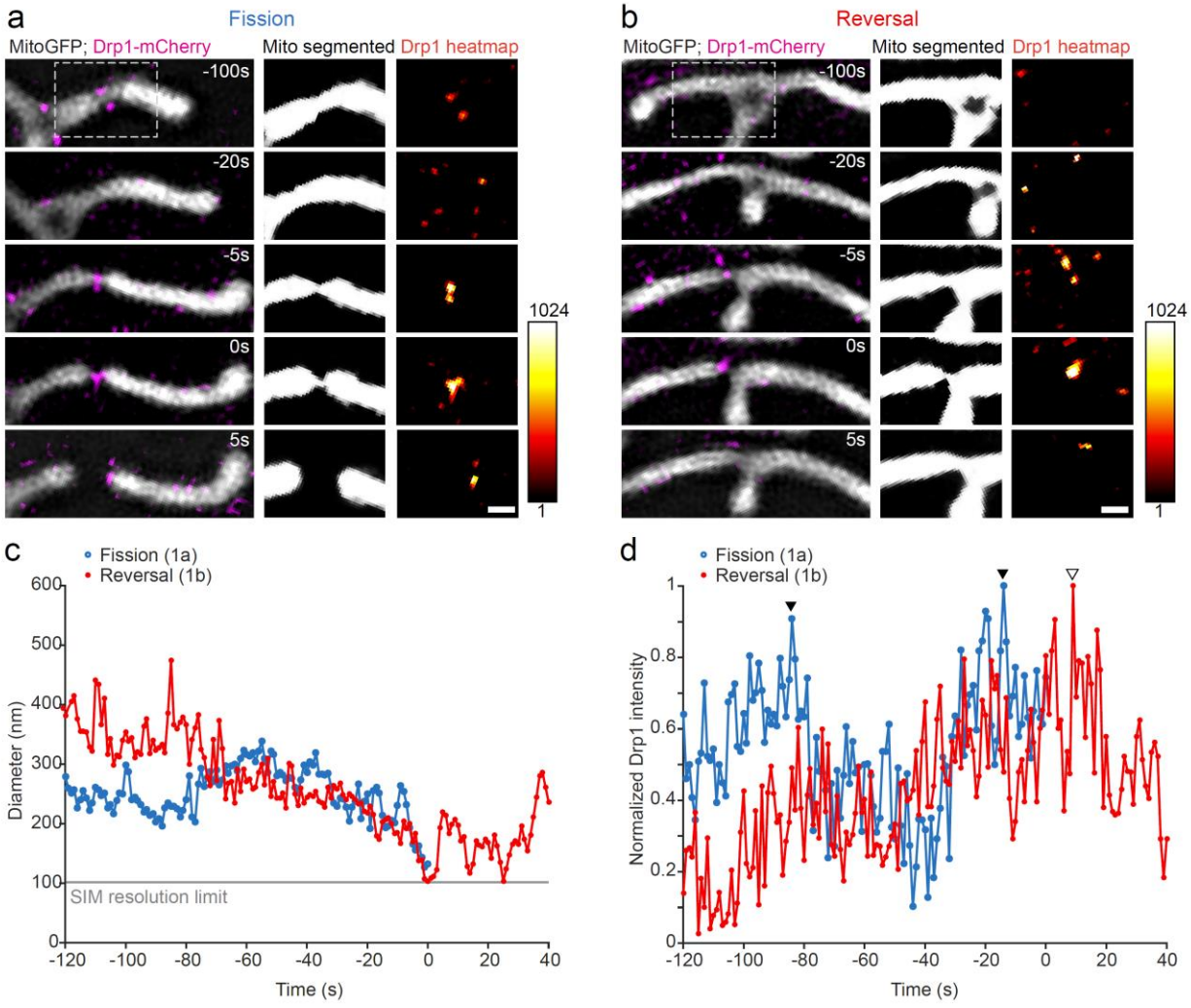

Figure 1: Drp1 intensity and constriction diameters at constriction sites. (a,b) Time-lapse SIM imaging of COS-7 cells transiently transfected with mito-GFP (grey) and mCh-Drp1 (magenta) showing (a) fission and (b) reversal events (see Movies S1,2, SFig 1). (c) Dynamic evolution of diameter at the mitochondrial constriction site measured for fission (blue) and reversal (red) events shown above. (d) Normalized integrated intensity of Drp1 at the constriction site over time measured for fission (blue) and reversal (red) events shown above. Arrowheads indicate rounds of Drp1 constriction (filled for fission, hollow for reversal). Scale bar represents 500 nm in a and b.

Presence of the division machinery does not ensure fission

To exclude the possibility that reversals are simply caused by differences in the fission machinery, we first investigated the presence of key molecular players for mitochondrial constriction – ER, Drp1 and Dyn2 (Figures 1 and 2). First, we examined the colocalization between the ER and mitochondrial constrictions, as such contacts mark pre-constrictions which can become fission sites [9]. We found that both fissions and reversals occurred at ER contact sites (Fig. 2a, c). Next, we examined the recruitment of the central molecular player Drp1; by quantifying the integrated intensity of Drp1, we found that its accumulation at constriction sites was similar for fissions and reversals (Fig. 1a, b, d, Fig. 2c). An accumulation of Drp1 typically coincided with an increased rate of constriction, measured at ~17 nm/s for fissions and 18 nm/s for reversals during the 5 seconds leading up to maximal constriction. Some sites underwent multiple rounds of constriction and relaxation, coupled with Drp1 accumulation and disassembly (Fig. 1d, arrowheads). Both fissions and reversals sometimes displayed cyclic dynamics, 3±2 constriction cycles/min and 2±1 cycles/min respectively (N=61 and 38), implying that cyclic activity does not distinguish fissions from reversals.

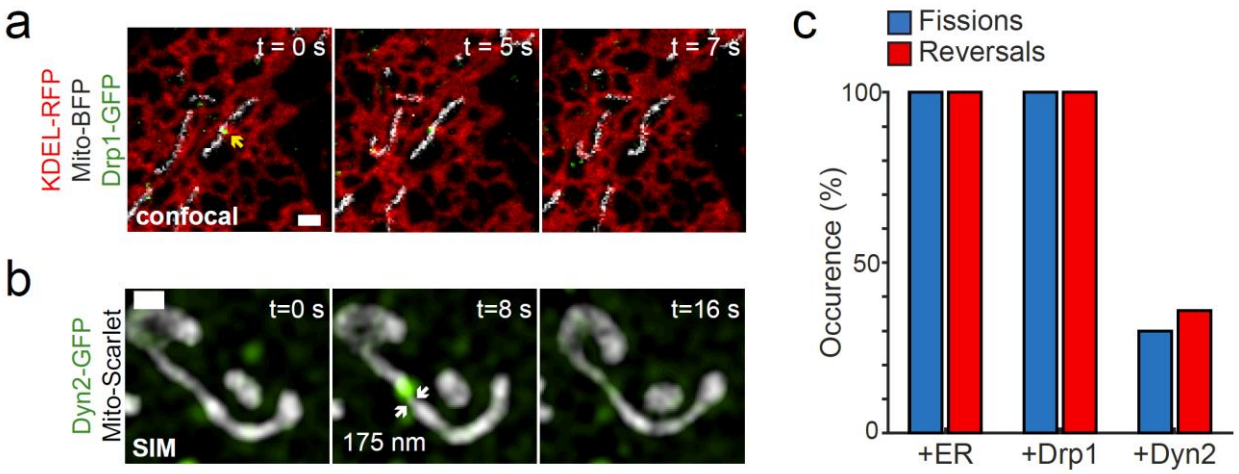

Figure 2: Presence of division machinery does not ensure successful fission. (a) Time-lapse live-cell confocal imaging of COS-7 cells transfected with Mito-BFP, Drp1-GFP and KDEL-RFP showing an example of reversal events in the presence of ER. Arrows indicate Drp1 mediated constrictions that reverse without dividing. (b) Time-lapse SIM imaging of mitochondria and Dyn2 showing a reversal in the presence of Dyn2. (c) Bar charts indicating the fraction of fissions and reversals observed in the presence of the ER, Drp1 and Dyn2. Scale bar represents 1 µm in (a) and 500 nm in (b).

Since Dyn2 has been implicated in mitochondrial fission [22], we also investigated whether its presence distinguishes fissions from reversals. Since our SIM imaging was limited to two colors, we performed fast (1 Hz), three-color live-cell confocal imaging of mitochondria, Drp1 and Dyn2. We observed both fissions and reversals, but found that Drp1 and Dyn2 could be present in both classes of constrictions. To determine whether these events satisfied our definition of reversals, we used the higher resolution of SIM to image mitochondria and Dyn2 (Fig. 2b).

Constriction sites which reversed in the presence of Dyn2 also reached diameters down to ~130 nm. Among mitochondrial division sites, we observed that 30% were enriched in Dyn2 (N=30) (Fig. 2c), consistent with recent reports that Drp1, but not Dyn2 is necessary for mitochondrial division [23]. Overall, no significant differences in the recruitment of mitochondrial division machinery were observed between fissions and reversals, including ER which defines the preconstriction, nor Drp1 and Dyn2 - the two most downstream components of the division machinery (Fig. 2c). This led us to hypothesize that both fissions and reversals are distinct outcomes of a shared, but non-deterministic process.

Fission events are characterized by higher bending energy

The different components of the division machinery combine at the constriction site to deform the organelle. While we found no difference in the presence of components of the fission machinery between fissions and reversals, we considered that there could be differences in the resulting deformation of the mitochondrial membrane. The resultant build-up of elastic energy is

an important physical precursor to the hemi-fission state that membranes transit before undergoing scission [27]. To investigate this, we quantified the minimal constriction diameters and local envelope curvatures at constriction sites, allowing us to compute the integrated bending energy.

We found that fissions and reversals do not differ in the minimal constriction diameter, since on average, constrictions leading to fission achieved measured diameters of 122 ± 3 nm (mean ± SEM, N = 69) in the frame before fission or maximal constriction respectively (defined as time t=0) (Fig. 3a), while reversals reached similar minimum diameters of 128 ± 4 nm (N = 43) (Fig. 3a). These sizes are consistent with the diameter at which Dnm1/Drp1 helix is proposed to assemble, encircling the mitochondrion [20, 28]. We also imaged mitochondria using live stochastic optical reconstruction microscopy (STORM), which offered higher spatial resolution but a reduced, ~6-second temporal resolution. Fission and reversal events measured by STORM had negligible differences in their minimum measured diameters, 90±18 (N=13) and 82±10 nm (N=10) respectively (SFig. 2a-c), marginally smaller than those measured by SIM. Our measurements are consistent with previously reported sizes of mitochondrial constrictions found with photoactivated localization microscopy (PALM) [29] and STORM [30]. Thus, within the resolution of SIM and STORM, we found no significant differences in minimal diameter between fissions and reversals.

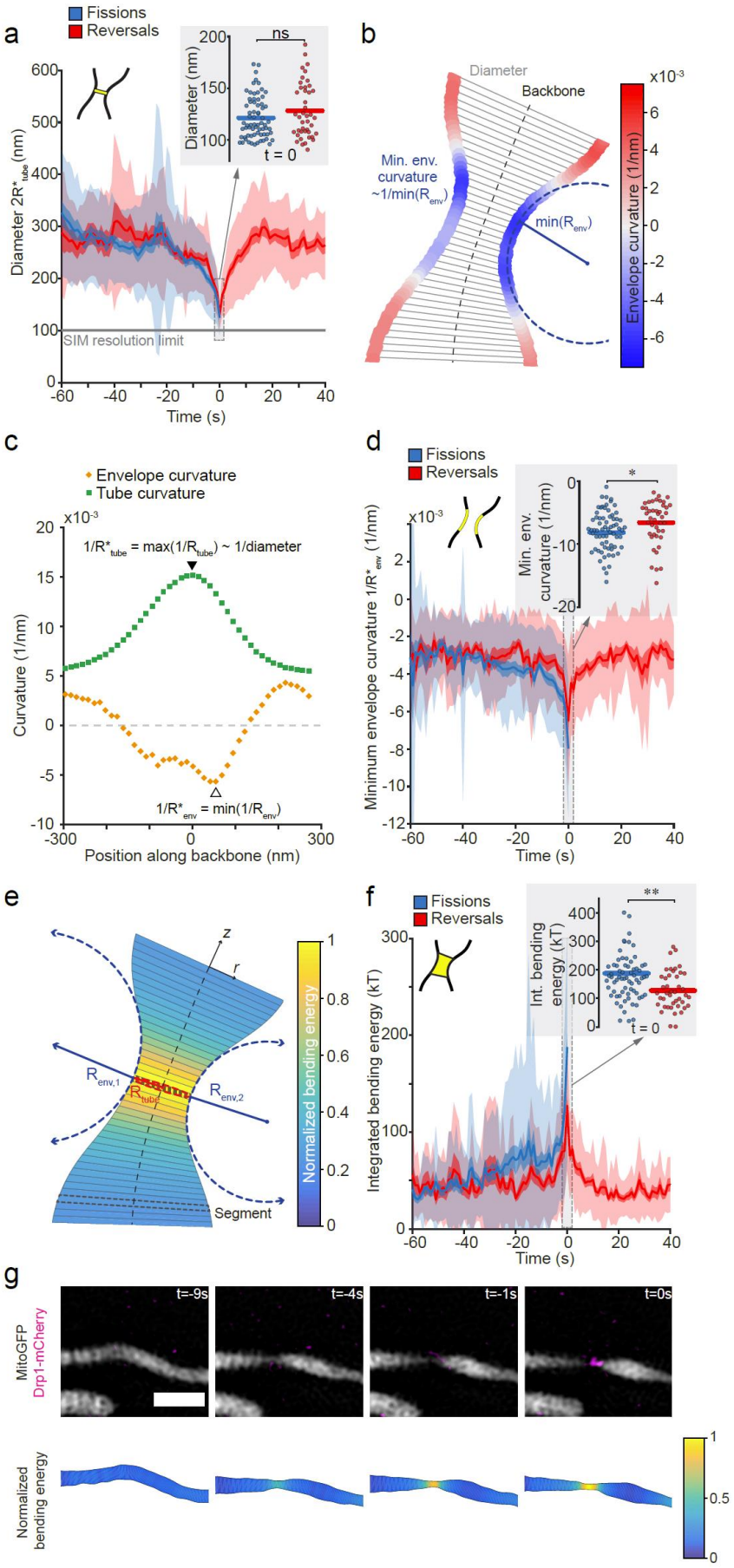

Figure 3: Curvature and bending energy at the constriction site for fissions and reversals. (a) Binned curves showing the evolution of the constriction diameter for fissions (blue, n=69) and reversals (red, n=43). Inset shows the distribution of minimal diameters of fission and reversals at t=0 (horizontal line shows mean). (b) Schematic showing the local envelope curvature at a constriction site (colormap). (c) Tube curvature and envelope curvature measured along the backbone at the constriction site in (a). (d) Binned curves showing the evolution of envelope curvature at the constriction site for fissions (blue, n=69) and reversals (red, n=43). Shaded regions represent SD (light shade) and SEM (dark shade). Inset shows the distribution of minimal envelope curvatures of fission and reversals at t=0 (horizontal line shows mean). (e) Schematic showing the bending energy measurement. The local envelope curvature R_{env} was computed as the local mean of opposing sides $R_{env,1}$ and $R_{env,2}$. Analysis of the local tube (R_{tube}) and envelope (R_{env}) radii for individual segments (striped region) allowed estimation of the local bending energy (colormap). (f) Binned curves for the calculated local bending energies over time for fissions (blue, n=70) and reversals (red, n=43). Shaded regions represent SD (light shade) and SEM (dark shade). Inset shows the distribution of integrated bending energies at the constriction site of fission and reversals at t=0 (horizontal line shows mean). (g) Timelapse showing the raw data (top) and estimated local bending energies (bottom, colormap) of a Drp1 mediated constriction site resulting in fission. Scale bar: 1um. Statistical significance calculated by 2-tailed Mann Whitney U test: n.s. P>0.05, *P<0.05, **P<0.01.

However, the energetic cost of membrane deformation is a function of the two principal membrane curvatures (Fig. 3b). We wondered whether fission and reversal sites could differ in membrane bending energy; to test this idea, we measured the, using our custom written analysis software (SFig. 6). The local curvatures exhibited extrema at the constriction site: a maximal tube curvature ($1/R^*_{tube}$) – related to the diameter – and a minimal envelope curvature ($1/R^*_{env}$) (Fig. 3c).

Indeed when we monitored the time evolution of the curvature extrema we found that distributions of envelope curvatures ($1/R_{env}$) were initially similar for fissions and reversals (Fig. 3d), but beginning at t ~ -30 seconds, deformations leading to fission achieved and maintained a lower minimum envelope curvature ($1/R^*_{env}$) on average: at t=0, $(-8.1 \pm 0.4) \cdot 10^{-3}$ nm^{-1} compared to $(-6.6 \pm 0.5) \cdot 10^{-3}$ nm^{-1} in the case of reversals (Fig. 3d inset, N=69 and 43 respectively). This difference in shape implies a difference in bending energy at mitochondrial constriction sites (see SI Methods). A single membrane may be modeled as an elastic sheet, whose bending energy, E_B, is given by the Helfrich equation [31] (Fig. 3e). To calculate the bending energy, we numerically evaluated

$$E_B(z) = \frac{\kappa_B}{2} \iint J^2 dA \qquad (1)$$

Here, κ_B is the membrane bending rigidity and J is the sum of local principal curvatures $J = \left(\frac{1}{R_{tube}} + \frac{1}{R_{env}}\right)$ measured for each segment along the mitochondrion and numerically integrated over the surface of the constriction site (Fig. 3e).(Fig. 3e, SI). The mitochondrial envelope is composed of two membranes, which are constrained to be in close proximity at the constriction site [32]. Thus, as a first approximation, we considered both membranes as a composite system with a rigidity of 40 k_BT, double the value of single lipid bilayers from *in vitro* measurements [33].

We followed the temporal evolution of the bending energy at the constriction site (Fig. 3f, g, Movie S3, SFig. 2d-f) and estimated the energy of the constriction site as a whole by summing the local contributions over its area (Fig. 2f). As seen for the envelope curvatures, the time evolution of the bending energy was similar for fissions and reversals until t ~ -30 seconds, when the distribution shifted to higher values for constrictions resulting in fission (Fig 3f inset, 188±14 k_BT versus 127±10 k_BT mean±SEM, N=70 and 43 respectively, Appendix A). This result might at first appear obvious, since constrictions resulting in fission must eventually overcome the energy barrier, while reversals do not. However, there is significant overlap between the distributions (Fig. 3f, inset), and a range of values of constricted state bending energies can result in either outcome (SFig. 2g,h). We wondered whether other contributions to the membrane elastic energy besides bending might contribute, and help to distinguish fissions and reversals.

Fission events are characterized by increased membrane tension

We noticed that after division, daughter mitochondria would recoil from each other, in a directed manner away from the division site (Fig. 4a), as if they were pulled in opposite directions. This coordinated motion was distinct from typical, sporadic mitochondrial mobility and was consistent

with what one would expect when cutting an elastic body under tension (Movie S4, S5). Membrane tension also contributes to the membrane elastic energy at the constriction site [31] and has been previously proposed to play a role in mitochondrial division [34]. Therefore, we next wanted to examine whether fission events occurred on mitochondria under higher membrane tension compared to mitochondria whose constriction sites reverse.

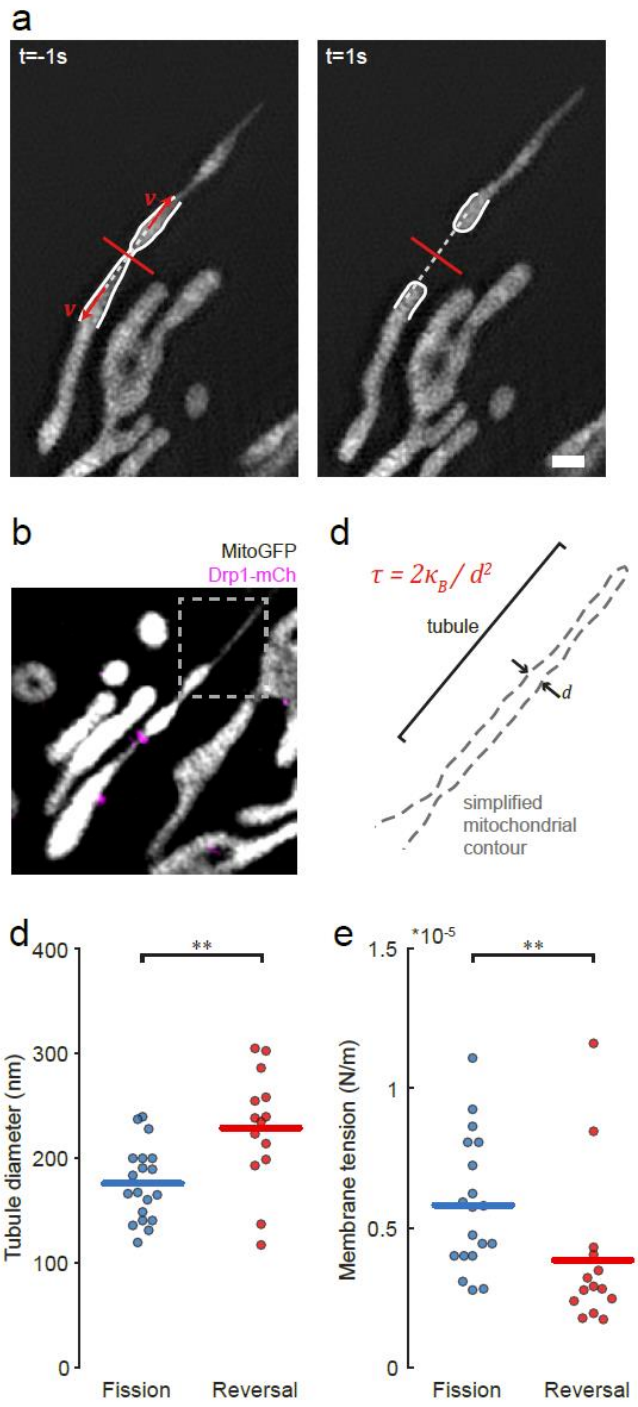

Figure 4: Estimated membrane tension for fissions and reversals. (a) Time-lapse SIM images of a mitochondrion (mito-GFP) 1 sec before (left) and after (right) fission showing the recoil of daughter mitochondria post fission. Measured retraction velocities $\boldsymbol{v}$ (red arrows) were projected perpendicular to the constriction site (white dashed line). (b) Fluorescence image showing a constricted mitochondrion with a pulled membrane tube (boxed region). Scale bar: 1 µm. (c) Mitochondrial contour from the outlined region in (a) showing the diameter of the tube d, used as a readout for tension τ. (d) Distribution of tubule radii measured between fission and reversal events. (e) Distribution of calculated membrane tension values between fission and reversal events. Statistical significance calculated by 1- and 2-tailed Mann-Whitney U test where appropriate: **P<0.01.

In vitro experiments can be used to estimate membrane tension by exerting a pulling force on a membrane and measuring the size of the resulting membrane tubule [35, 36]. Analogously, in living cells, mitochondria can exhibit membrane tubules, which are dynamic, reversible structures spontaneously pulled out by microtubule-based motors [37, 38] (Fig. 4b). These structures were observed at similar frequencies just before fissions or reversals (19% and 24% for N=101 and 59 respectively). We can infer the membrane tension by assuming it minimizes the elastic energy of cylindrical membrane, in which case the diameter of the tube d is related to the membrane tension τ and the membrane bending rigidity κ_B [35, 36] (Fig. 4c, SI):

$$\tau = \frac{2\kappa_B}{d^2} \qquad (2)$$

The average diameters of tubules pulled from mitochondria that subsequently either divided or reversed were 176 ± 4 nm and 229 ± 7 nm respectively (Fig. 4d). According to equation (2), the population of mitochondria undergoing fission was under significantly higher average membrane tension at 5.81 ± 0.54 x 10^{-6} N/m, compared to the population undergoing reversals at 3.85 ± 0.75 x 10^{-6} N/m (Fig. 4e, N = 19 and N = 14 respectively, mean ± SEM). The recoil motion also allowed us to independently estimate membrane tension in individual mitochondria, with results consistent with those estimated from membrane tubules (SI, Fig. 4e). These results suggest that constricted mitochondria at higher membrane tensions are more likely to subsequently divide.

As further evidence for excess membrane tension, we observed pearling modes on 11% of dividing mitochondria (N=88) (SFig. 9e), also previously reported in neuronal mitochondria [39, 40]. We found that mitochondria exhibiting pearling modes eventually underwent fission of at least one of the constriction sites (100%, N=10). Conversely, reversals of pearling modes were rarely observed (4%, N=57) and occurred exclusively following fission at a neighboring

constriction site, suggesting that the loss of tension released during fission could be responsible (SFig. 9e, Movie S4, S5). Overall, these results speak to the role of membrane tension as increasing the likelihood that mitochondrial constrictions divide.

Reduced membrane tension decreases the probability of fission

Next we set out to explore underlying mechanisms for differences in membrane tension between mitochondria. The presence of recoil after division suggests external forces are present and pulling the mitochondria in opposite directions, which could give rise to an increased membrane tension. Mitochondrial transport is mainly mediated through microtubule-based motor proteins [41], and we hypothesized that the same motors could exert an external pulling force and generate membrane tension. To test this hypothesis, we depolymerized microtubules using nocodazole [42, 43]. Indeed, while cell and organelle morphologies were maintained (Fig. S3), we observed a decrease in recoil velocities reflected in a reduction of estimated membrane tensions by 40% (Fig. 5a, N=33 control and 26 nocodazole).

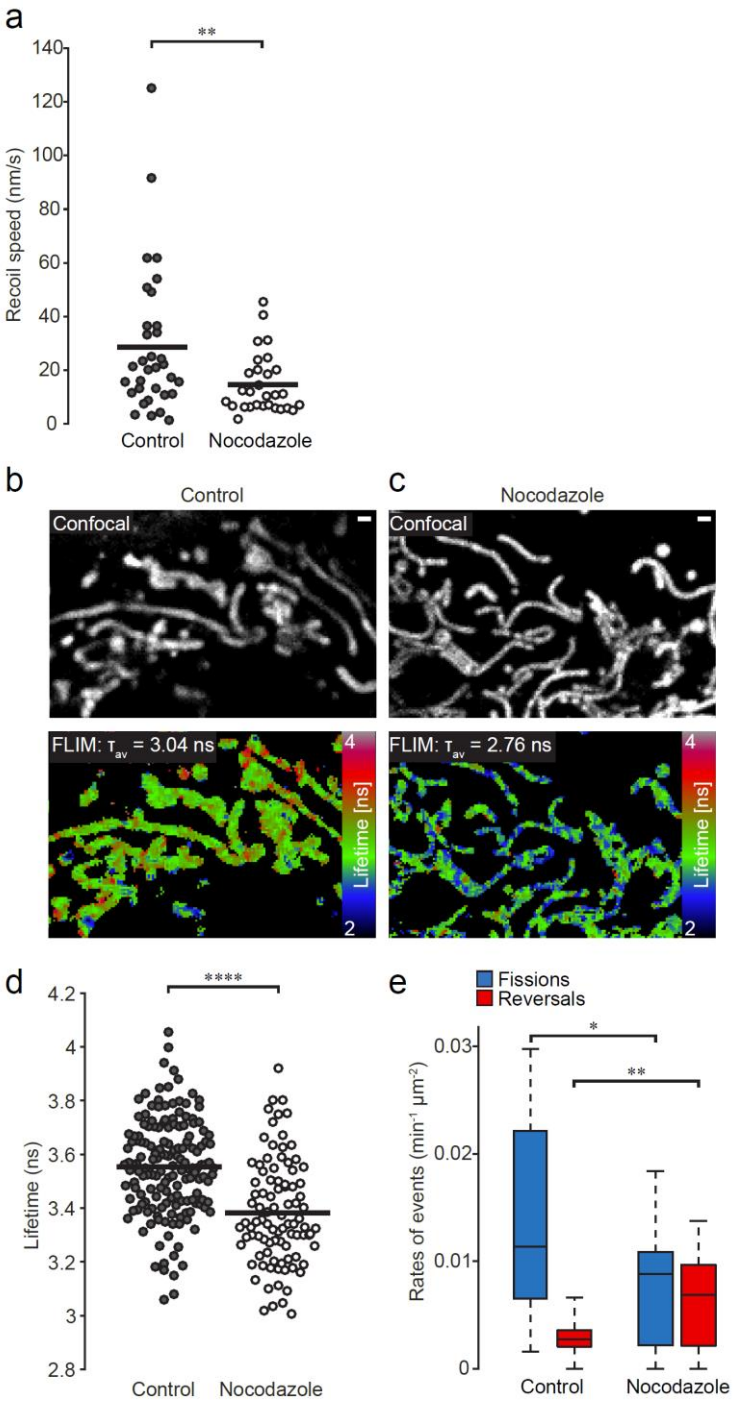

Figure 5: Membrane tension under nocodazole perturbation. (a) Distribution of recoil speeds of mitochondria post-division, between control and nocodazole treated cells. (b) Confocal (up) and FLIM (down) images of mitochondria in control cells marked with the FliptR fluorescent tension probe. (c) Confocal (up) and FLIM (down) images of mitochondria in nocodazole treated cells marked with the FliptR fluorescent tension probe. (d) Distributions of bulk fluorescence lifetimes of the FliptR fluorescent tension probe between control and nocodazole treated cells. (e) Box chart showing rates of fission and reversal in Nocodazole treated (N=16) and control (N=16) cells. Scale bars: 1µm. Statistical significance calculated by 1- and 2-tailed Mann-Whitney U test where appropriate: *P<0.05, **P<0.01, ****P<0.0001.

To prove that depolymerizing the microtubule cytoskeleton directly results in a decreased membrane tension, we used a mitochondrial targeting variant of the mechanosensitive FliptR probe (Fig. 5b,c, SFig. 3a)[44-46]. The fluorescence lifetime of FliptR depends on the orientation between its chromophoric groups, which is sensitive to membrane tension. Comparing cells under control versus nocodazole-treated conditions, FliptR showed significantly shorter average fluorescence lifetimes, indicative of an overall reduction in membrane tension (Fig. 5d).

After establishing that nocodazole treatment reduced mitochondrial membrane tension, we examined its consequences on mitochondrial division. Importantly, the rate of Drp1-induced constrictions per mitochondrial area was unperturbed by nocodazole treatment (~ 0.014 $\mathrm{min}^{-1}\mu\mathrm{m}^{-2}$). Furthermore, the degree of overlap between mitochondria and ER remained unchanged (SFig. 3b-f), as did mitochondrial membrane potential and diameter (SFig. 3g,h). However, we found a 2.4-fold increase in the rate of reversal events (Fig. 5e), and a concomitant decrease in the rate of fission. These results suggest that Drp1 activity is unchanged by nocodazole treatment, and that decreased membrane tension leads to a reduced likelihood of a constriction site to divide.

Probabilistic model for mitochondrial fission

Our measurements show that fission occurs over a wide range of bending energies, membrane tensions, and timescales. Models developed for other fission processes, such as dynamin-mediated endocytosis, explain the distribution of fission times as an outcome of a stochastic process [47] in which thermal fluctuations allow the membrane to overcome the energy barrier to fission. Constricted membranes with higher elastic energy, and thus a lower residual energy barrier, will

be more likely to undergo fission. Conversely, sites with lower bending energies will be further away from the energy barrier to fission, making it more likely for the fission machinery to disassemble within this timeframe, and lead to reversal. In such a stochastic fluctuation-activated model, the probability $p(E)$ to overcome the energy barrier to fission E_f, given a certain membrane energy $E \in [0, E_f]$ is set by:

$$p(E) = \exp\left(-\frac{\Delta E}{\lambda}\right) = \exp\left(\frac{E-E_f}{\lambda}\right) \quad (3)$$

Since bending increases the energy of the constricted state, it brings constrictions closer to the energy required for fission, implying that constrictions with higher bending energy will be more likely to divide. This idea is supported by the experimentally measured probability of fission, defined as the ratio of the number of fissions to total constrictions with a given energy, which increases with local bending energy and closely matches the relationship given by equation (3) (Fig. 6a).

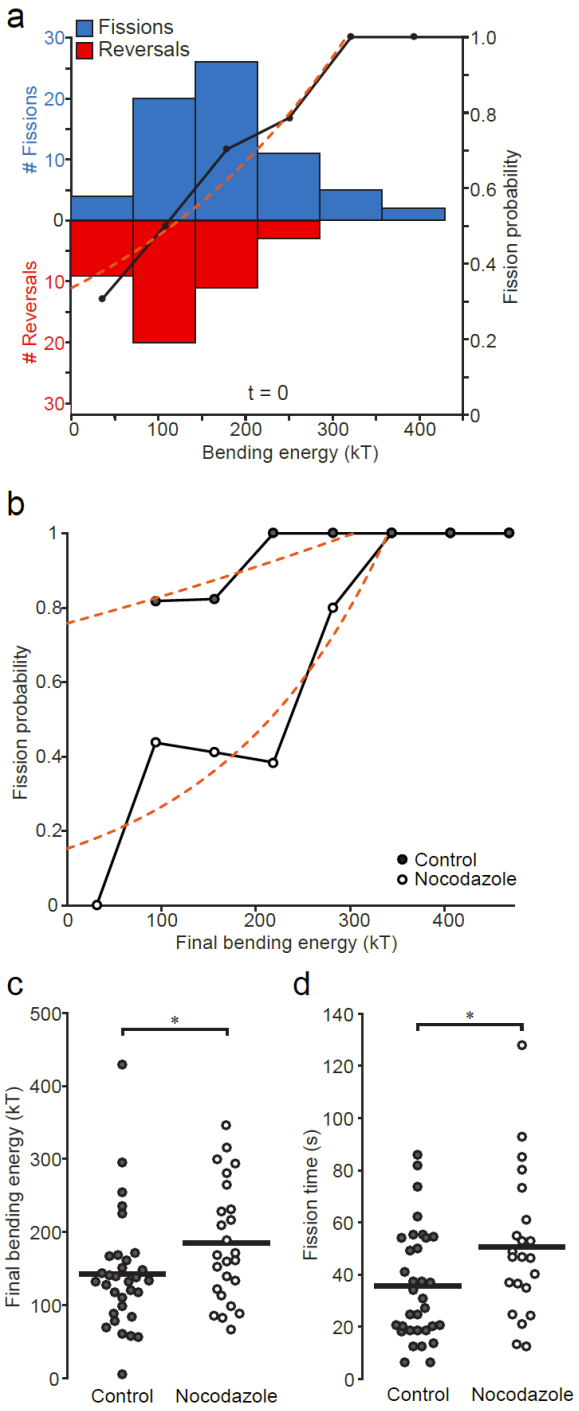

Figure 6: Fission timing and probability related to bending energy and tension. (a) Left: Histogram showing numbers of fissions and reversals at different local bending energy intervals. Right: Experimental probability of fission calculated as ratio of fissions to total constrictions at different local bending energy intervals. Fit curve (red dashed line) $y = a\exp(bx)$, with $a = 0.336$ and $b = 0.0035\ kT^{-1}$ (b) Experimental probability of fission of control and nocodazole treated cells. Fits (red dashed line) $= a\exp(bx)$, with $a = 0.758$ and $b = 0.00091\ kT^{-1}$ for control and $a = 0.1528$ and $b = 0.00553\ kT^{-1}$ for nocodazole respectively. (c) Distribution of final bending energies between control and nocodazole treated fission events. (d) Distribution of fission times between control and nocodazole treated fission events. Statistical significance calculated by 1- and 2-tailed Mann-Whitney U test where appropriate: *P<0.05.

Importantly, fitting the experimental probability of fission to equation (3) allowed us to estimate the fluctuation energy and the energy barrier to fission (Fig. 6a). From the fit to equation (3) we found an energy barrier E_f ~ 250-300 k_BT, corresponding to the deformation energy above which we expect deterministic fission and $p(E)\sim1$ (Fig 6a). Considering that mitochondria are double-membraned organelles, this value is consistent with previous simulations for dynamin-mediated scission [47], as well as theoretical estimates of the energy barrier to a hemifission state, which spontaneously leads to fission [27]. Similarly, considering the time required to undergo fission, we estimated the fluctuation energy at λ ~90 k_BT (SI, SFig. 4f). Consistent with this, we estimated the residual energy barrier, ΔE ~ 90 k_BT as the difference between the estimated energy barrier and the average constriction site energies (SI). This is far too large a barrier to be frequently overcome by thermal fluctuations alone, so what could account for this fluctuation energy?

Previous work has shown that membrane tension has the effect of lowering the energy barrier to fission [47]. From another point of view, a membrane under tension can stretch, producing small changes in its surface area [31, 48], which contribute to its elastic energy. Consequently, stretching energy could contribute to overcome the residual energy barrier, ΔE, between the constricted and hemi-fission states. Since the external forces acting on a mitochondrion are fluctuating in time, the membrane tension and therefore elastic energy at the constriction site will also fluctuate. Considering the values we found for membrane tension (Fig. 4d, SI), we estimated the stretching energy to contribute ~50 kT, consistent across two independent estimates (SI). This nearly matches the fluctuation energy, λ estimated above (SI); we thus propose that membrane tension could act as a fluctuating source of energy, enabling constriction sites to overcome the energy barrier to fission. If this is the case, reducing the membrane tension by nocodazole treatment should reduce

the values we extract for λ. Fitting equation (3) to both datasets indeed shows that while the barrier to fission remains mostly unchanged, the size of the energy fluctuations working to overcome the barrier was decreased as predicted, by 6-fold. Examining the measured probability of fission between control and nocodazole treated cells, we found it was shifted towards higher bending energies when membrane tension is decreased (Fig 6b). This is consistent with our model, since achieving a similar probability of fission would now require more deformation to increase the energy of the constricted state (Fig. 6c, N=33 control and 22 nocodazole). We also noticed that Drp1 appeared to reside for longer time periods at mitochondrial constriction sites in nocodazole-treated cells. Fission events in nocodazole-treated cells required on average ~12±7 s longer (Fig. 6d, N=33 control and N=22 nocodazole), reflecting decreased fission probability and consistent with a major role for membrane tension in driving the final step of fission.

Discussion

We propose a model based on an energy landscape for the mitochondrial fission reaction, where membrane bending energy and tension determine the probability of overcoming an energy barrier (Fig 7a). Bending induced by the constriction machinery (Fig. 7b), increases the energy at the constriction site. Separately, membrane tension – largely accounted for by the microtubule cytoskeleton - determines the range of fluctuation energies available to overcome the energy barrier (Fig. 7b). Since constrictions cannot be maintained indefinitely, if during their lifetime they do not experience a large enough fluctuation, they will become reversals. As predicted, with a nocodazole-induced decrease in membrane tension, there are fewer fluctuations large enough to overcome the fission barrier, which lowers the probability of fission and results in a larger proportion of reversals. Our physical model is intended to account for how mitochondria integrate

the forces exerted by the molecular fission machinery to decide whether and when to divide, in a manner that is independent of the precise origin of the forces. Hence, the model helps explain the observed variability in the mitochondrial division machinery by proposing a more general framework accounting for the energetic cost of mitochondrial deformation.

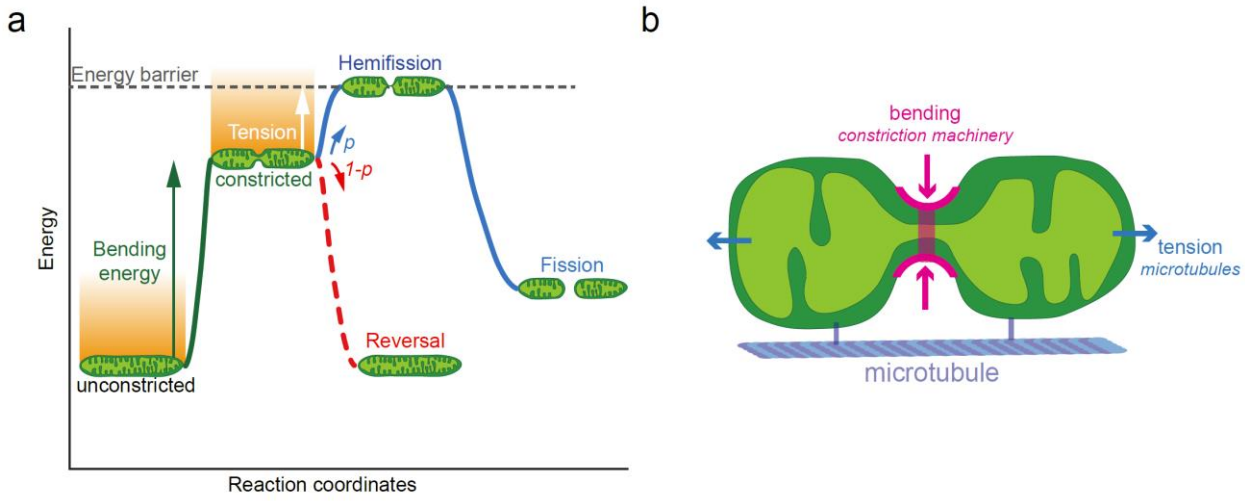

Figure 7: Physical model of mitochondrial fission controlled by bending energy and membrane tension. (a) Cartoon of the probabilistic model of mitochondrial fission showing the contribution of bending energy (green line) and membrane tension (orange shaded area) in reaching the energy barrier for fission (grey dashed line). Both bending energy and tension set the probability p of fission (blue line). Reversals occur either due to a lack of bending energy or low probability of necessary fluctuation energies. (b) Schematic representation of the different contributions to fission probability: bending energy (magenta) and tension (blue).

Mitochondrial fission differs from other fission processes such as dynamin mediated endocytosis for which physical models have been developed [47]. Firstly, there are significant differences in the sizes and geometries of tubular mitochondrial constrictions compared to buds involved in dynamin mediated endocytosis, suggesting that different mechanisms might be at play. Indeed, our results suggest that thermal fluctuations are insufficient for driving mitochondrial fission. Instead, we propose that larger energy fluctuations due to membrane tension are responsible for

overcoming the energy barrier to fission. Secondly, mitochondrial division requires the scission of two membranes. To model fission probabilities, we consider the two membranes as coupled together [49] forming a composite elastic sheet with a mean geometry, but a closer look reveals additional insights into the interplay between the two membranes (SFig 5, SI). Because the bending energy of the inner membrane is geometrically constrained to be higher, we expect it to undergo fission first (SI, SFig. 5). Fission of the outer membrane could then follow due to a sudden increase in the local stress, since it must now bear the load previously shared with the inner membrane. Sequential timing guarantees a non-leaky fission process, which is predicted for mitochondria [50] to avoid inadvertently triggering apoptosis or disruption of membrane potential [51].

The probabilistic nature of mitochondrial fission and the prevalence of reversals may play a role in regulating global mitochondrial network morphologies. Given the highly crowded intracellular environment, the resulting mechanical forces could recruit the mitochondrial division machinery in an unregulated manner, leading to fragmentation of the network [25]. Our model provides insight into how by modulating tension, the degree of fragmentation might be regulated. Furthermore, our results could explain how remodeling of the microtubule cytoskeleton during the cell cycle could help to regulate the global mitochondrial morphology and proliferation through changes in mitochondrial membrane tension.

Maintaining the quality and distribution of the mitochondrial population requires regulating the division of individual mitochondria. How individual mitochondria are primed for division could involve adapting their intrinsic properties to locally influence the probability of fission. For example, the accumulation of negatively curved lipids – such as cardiolipin [52] - at the constriction site could generate negative envelope curvature to promote fission. Indeed, a dominant negative Drp1-mutation, which does not interact with cardiolipin, leads to lower fission rates [53].

Furthermore, increases in Ca2+ leading up to mitochondrial division [12, 40, 54] could change the local mechanical properties at the constriction site[55], facilitating division. Finally, mitochondrial division has been observed to take place near replicating nucleoids [56] – the presence of which might create 'rigid islands' that increase bending energies at adjacent constriction sites [57], making them more likely to divide according to our model. Such internal mechanisms could simultaneously control the positioning and fate of mitochondrial constrictions.

Acknowledgements

We would like to thank Hélène Perreten for technical assistance, Dr. Hari Shroff for the mitoGFP construct and Dr. Gia Voeltz for the Drp1 and Dyn2 constructs. We would like to thank Niklas Berliner, Jennifer Lippincott Schwartz, Simon Schutz and Dr. Tobias Schneider for helpful discussions. Imaging data used in this publication was produced in collaboration with the Advanced Imaging Center, a facility jointly supported by the Gordon and Betty Moore Foundation and HHMI at HHMI's Janelia Research Campus. We thank Lin Shao and Teng-Leong Chew at Janelia AIC for their help with SIM imaging. We thank Benoit Kornmann, Qian Feng, Thomas Misgeld and Leanne Godinho for comments on the manuscript. Research in S.M.'s and A.R.'s laboratories is supported by the National Centre of Competence in Research Chemical Biology. T.K. received funding from European Molecular Biology Organization (ALTF-739-2016) and the Munich Cluster for Systems Neurology (SyNergy).

Author contributions

Conceptualization, D.M., L.C., T.K., A.R., S.M.; Methodology, D.M., L.C., T.K., A.R., S.M.; Software, D.M., L.C.; Validation, D.M., L.C., T.K.; Formal Analysis, D.M., L.C., A.C.; Investigation, D.M., L.C., T.K., A.C.; Resources, A.C., A.G., S.Mat., A.R.; Data Curation, D.M. L.C.; Writing – Original Draft, D.M., L.C., S.M.; Writing – Review and Editing, D.M., L.C., T.K., A.C., A.G., S.Mat., A.R., S.M.; Visualization, D.M., L.C., T.K.; Supervision, A.R., S.M.; Project Administration S.M.; Funding Acquisition, T.K., S.M.

Declaration of interests

The original FliptR probe (not targeted to mitochondria), is sold by Spirochrome through the NCCR website, from which the NCCR receives 15% of the profits.

References

1. Nunnari, J., et al., *Mitochondrial transmission during mating in Saccharomyces cerevisiae is determined by mitochondrial fusion and fission and the intramitochondrial segregation of mitochondrial DNA.* Molecular biology of the cell, 1997. **8**: p. 1233-1242.
2. Youle, R.J. and A.M. van der Bliek, *Mitochondrial Fission, Fusion, and Stress.* Science, 2012. **337**: p. 1062-1065.
3. Tondera, D., et al., *SLP-2 is required for stress-induced mitochondrial hyperfusion.* The EMBO Journal, 2009. **28**: p. 1589-1600.
4. Gomes, L.C., G.D. Benedetto, and L. Scorrano, *During autophagy mitochondria elongate, are spared from degradation and sustain cell viability.* Nature Cell Biology, 2011. **13**: p. 589-598.
5. Rambold, A.S., et al., *Tubular network formation protects mitochondria from autophagosomal degradation during nutrient starvation.* Proceedings of the National Academy of Sciences, 2011. **108**: p. 10190-10195.
6. Mitra, K., et al., *A hyperfused mitochondrial state achieved at G1-S regulates cyclin E buildup and entry into S phase.* Proceedings of the National Academy of Sciences of the United States of America, 2009. **106**: p. 11960-5.
7. Twig, G., et al., *Fission and selective fusion govern mitochondrial segregation and elimination by autophagy.* The EMBO Journal, 2008. **27**: p. 433-446.
8. Burman, Jonathon L., et al., *Mitochondrial fission facilitates the selective mitophagy of protein aggregates.* J Cell Biol, 2017. **216**: p. 3231-3247.
9. Friedman, J.R., et al., *ER tubules mark sites of mitochondrial division.* Science, 2011. **334**: p. 358-362.
10. Korobova, F., V. Ramabhadran, and H.N. Higgs, *An Actin-Dependent Step in Mitochondrial Fission Mediated by the ER-Associated Formin INF2.* Science, 2013. **339**: p. 464-467.
11. Manor, U., et al., *A mitochondria-anchored isoform of the actin-nucleating spire protein regulates mitochondrial division.* eLife, 2015. **4**.
12. Ji, W.K., et al., *Actin filaments target the oligomeric maturation of the dynamin GTPase Drp1 to mitochondrial fission sites.* eLife, 2015. **4**.
13. Palmer, C.S., et al., *MiD49 and MiD51, new components of the mitochondrial fission machinery.* EMBO reports, 2011.
14. Gandre-Babbe, S. and A.M. van der Bliek, *The novel tail-anchored membrane protein Mff controls mitochondrial and peroxisomal fission in mammalian cells.* Molecular biology of the cell, 2008. **19**: p. 2402-12.
15. Otera, H., et al., *Mff is an essential factor for mitochondrial recruitment of Drp1 during mitochondrial fission in mammalian cells.* Journal of Cell Biology, 2010.
16. Mozdy, A.D., J.M. McCaffery, and J.M. Shaw, *Dnm1p GTPase-mediated mitochondrial fission is a multi-step process requiring the novel integral membrane component Fis1p.* Journal of Cell Biology, 2000. **151**: p. 367-379.
17. Labrousse, A.M., et al., *C. elegans dynamin-related protein DRP-1 controls severing of the mitochondrial outer membrane.* Molecular Cell, 1999. **4**: p. 815-826.
18. Smirnova, E., et al., *Dynamin-related Protein Drp1 Is Required for Mitochondrial Division in Mammalian Cells.* Molecular Biology of the Cell, 2001. **12**: p. 2245-2256.

19. Ingerman, E., et al., *Dnm1 forms spirals that are structurally tailored to fit mitochondria.* Journal of Cell Biology, 2005. **170**: p. 1021-1027.
20. Mears, J.A., et al., *Conformational changes in Dnm1 support a contractile mechanism for mitochondrial fission.* Nature Structural & Molecular Biology, 2011. **18**: p. 20-26.
21. Fröhlich, C., et al., *Structural insights into oligomerization and mitochondrial remodelling of dynamin 1-like protein.* EMBO Journal, 2013. **32**: p. 1280-1292.
22. Lee, J.E., et al., *Multiple dynamin family members collaborate to drive mitochondrial division.* Nature, 2016. **540**: p. 139-143.
23. Kamerkar, S.C., et al., *Dynamin-related protein 1 has membrane constricting and severing abilities sufficient for mitochondrial and peroxisomal fission.* Nature Communications, 2018. **9**: p. 5239.
24. Koirala, S., et al., *Interchangeable adaptors regulate mitochondrial dynamin assembly for membrane scission.* Proceedings of the National Academy of Sciences, 2013. **110**: p. E1342-E1351.
25. Helle, S.C.J., et al., *Mechanical force induces mitochondrial fission.* eLife, 2017. **6**: p. e30292.
26. Legesse-Miller, A., *Constriction and Dnm1p Recruitment Are Distinct Processes in Mitochondrial Fission.* Molecular Biology of the Cell, 2003. **14**: p. 1953-1963.
27. Kozlovsky, Y. and M.M. Kozlov, *Membrane Fission: Model for Intermediate Structures.* Biophysical Journal, 2003. **85**: p. 85-96.
28. Basu, K., et al., *Molecular mechanism of DRP1 assembly studied in vitro by cryo-electron microscopy.* PLoS ONE, 2017. **12**: p. 1-21.
29. Rosenbloom, A.B., et al., *Optimized two-color super resolution imaging of Drp1 during mitochondrial fission with a slow-switching Dronpa variant.* Proceedings of the National Academy of Sciences, 2014. **111**: p. 13093-13098.
30. Shim, S.-H., et al., *Super-resolution fluorescence imaging of organelles in live cells with photoswitchable membrane probes.* Proceedings of the National Academy of Sciences, 2012. **109**: p. 13978-13983.
31. Helfrich, W., *No Title.* 1973. **28**: p. 3-7.
32. Hu, G.B., *Whole cell cryo-electron tomography suggests mitochondria divide by budding.* Microscopy and Microanalysis, 2014. **20**: p. 1180-1187.
33. Niggemann, G., M. Kummrow, and W. Helfrich, *The Bending Rigidity of Phosphatidylcholine Bilayers - Dependences on Experimental-Method, Sample Cell Sealing and Temperature.* Journal De Physique II, 1995. **5**: p. 413-425.
34. Klecker, T., et al., *The yeast cell cortical protein Num1 integrates mitochondrial dynamics into cellular architecture.* Journal of Cell Science, 2013. **126**: p. 2924-2930.
35. Evans, E. and A. Yeung, *Hidden dynamics in rapid changes of bilayer shape.* Chemistry and Physics of Lipids, 1994. **73**: p. 39-56.
36. Derényi, I., F. Jülicher, and J. Prost, *Formation and Interaction of Membrane Tubes.* Physical Review Letters, 2002. **88**: p. 4.
37. Huang, X., et al., *Kissing and nanotunneling mediate intermitochondrial communication in the heart.* Proc Natl Acad Sci U S A, 2013. **110**: p. 2846-2851.
38. Wang, C., et al., *Dynamic tubulation of mitochondria drives mitochondrial network formation.* Cell Research, 2015. **25**: p. 1108-1120.
39. Gonzalez-Rodriguez, D., et al., *Elastocapillary Instability in Mitochondrial Fission.* Physical Review Letters, 2015. **115**.

40. Cho, B., et al., *Constriction of the mitochondrial inner compartment is a priming event for mitochondrial division.* Nature Communications, 2017. **8**: p. 15754.
41. Boldogh, I.R. and L.A. Pon, *Mitochondria on the move*, in *Trends in Cell Biology*2007.
42. Hoebeke, J., G. Van Nijen, and M. De Brabander, *Interaction of oncodazole (R 17934), a new anti-tumoral drug, with rat brain tubulin.* Biochemical and Biophysical Research Communications, 1976. **69**: p. 319-324.
43. De Brabander, M.J., et al., *The Effects of Methyl [5-(2-Thienylcarbonyl)-1H-benzimidazol-2-yl]carbamate, (R 17934; NSC 238159), a New Synthetic Antitumoral Drug Interfering with Microtubules, on Mammalian Cells Cultured in Vitro.* Cancer Research, 1976. **36**: p. 905-916.
44. Soleimanpour, S., et al., *Headgroup engineering in mechanosensitive membrane probes.* Chemical Communications, 2016. **52**: p. 14450-14453.
45. Colom, A., et al., *A fluorescent membrane tension probe.* Nature Chemistry, 2018: p. 1-22.
46. Goujon, A., et al., *Mechanosensitive Fluorescent Probes to Image Membrane Tension in Mitochondria, Endoplasmic Reticulum, and Lysosomes.* Journal of the American Chemical Society, 2019: p. jacs.8b13189.
47. Morlot, S., et al., *Membrane shape at the edge of the dynamin helix sets location and duration of the fission reaction.* Cell, 2012. **151**: p. 619-629.
48. Wang, S., et al., *Membrane Deformability and Membrane Tension of Single Isolated Mitochondria.* Cellular and Molecular Bioengineering, 2008. **1**: p. 67-74.
49. Donzeau, M., et al., *Tim23 links the inner and outer mitochondrial membranes.* Cell, 2000. **101**: p. 401-412.
50. Ugarte-Uribe, B., et al., *Dynamin-related protein 1 (Drp1) promotes structural intermediates of membrane division.* Journal of Biological Chemistry, 2014. **289**: p. 30645-30656.
51. Hatch, A.L., P.S. Gurel, and H.N. Higgs, *Novel roles for actin in mitochondrial fission.* Journal of Cell Science, 2014. **127**: p. 4549-4560.
52. Stepanyants, N., et al., *Cardiolipin's propensity for phase transition and its reorganization by dynamin-related protein 1 form a basis for mitochondrial membrane fission.* Molecular Biology of the Cell, 2015. **26**: p. 3104-3116.
53. Montessuit, S., et al., *Membrane Remodeling Induced by the Dynamin-Related Protein Drp1 Stimulates Bax Oligomerization.* Cell, 2010. **142**: p. 889-901.
54. Chakrabarti, R., et al., *INF2-mediated actin polymerization at the ER stimulates mitochondrial calcium uptake, inner membrane constriction, and division.* Journal of Cell Biology, 2018. **217**: p. 251-268.
55. Kaasik, A., et al., *Regulation of mitochondrial matrix volume.* American Journal of Physiology-Cell Physiology, 2006. **292**: p. C157-C163.
56. Lewis, S.C., L.F. Uchiyama, and J. Nunnari, *ER-mitochondria contacts couple mtDNA synthesis with mitochondrial division in human cells.* Science, 2016. **353**: p. aaf5549.
57. Feng, Q. and B. Kornmann, *Mechanical forces on cellular organelles.* Journal of Cell Science, 2018. **131**: p. jcs218479.
58. Gustafsson, M.G.L., *Surpassing the lateral resolution limit by a factor of two using structured illumination microscopy.* Journal of Microscopy, 2000. **198**: p. 82-87.

59. Gustafsson, M.G.L., et al., *Three-Dimensional Resolution Doubling in Wide-Field Fluorescence Microscopy by Structured Illumination.* Biophysical Journal, 2008. **94**: p. 4957-4970.
60. York, A.G., et al., *Instant super-resolution imaging in live cells and embryos via analog image processing.* Nature Methods, 2013. **10**: p. 1122-1126.
61. Curd, A., et al., *Construction of an instant structured illumination microscope.* Methods, 2015. **88**: p. 37-47.
62. Richardson, W.H., *Bayesian-Based Iterative Method of Image Restoration**. Journal of the Optical Society of America, 1972. **62**: p. 55.
63. Lucy, L.B., *An iterative technique for the rectification of observed distributions.* The Astronomical Journal, 1974. **79**: p. 745.
64. Wolter, S., et al., *RapidSTORM: Accurate, fast open-source software for localization microscopy*, in *Nature Methods*2012. p. 1040-1041.
65. Trujillo-Ortiz, A., *DagosPtest - File Exchange - MATLAB Central.* 2015.
66. Cardillo, G., *mwwtest(x1,x2) - File Exchange - MATLAB Central.* 2015.

Materials and Methods

Cell culture, transfections and dye labelling.

Cos-7 cells were grown in Dulbecco's modified Eagle medium (DMEM) supplemented with 10% fetal bovine serum (FBS). Cells were plated on 25 mm, #1.5 glass coverslips (Menzel) 16-24 h prior to transfection at a confluency of ~10^5 cells per well. Dual transfections containing mCh-Drp1 (Addgene, plasmid #49152) and Mito-GFP (gift from Hari Shroff, Cox8a presequence) were performed with either Lipofectamine 2000 (Life Technologies) or using electroporation (BioRad Xcell). Lipofectamine transfections were carried out in Opti-MEM using 150 ng of mCh-Drp1, 150 ng of Mito-GFP and 1.5 µL of Lipofectamine 2000 per 100 µL Opti-MEM. Electroporation was performed using salmon sperm as a delivery agent. Briefly, cells were pelleted by centrifugation and resuspended in OPTI-MEM. Plasmids and sheared salmon sperm DNA were added to 200 µL of the cell suspension prior to electroporation using a Bio-Rad Gene Pulser (190 Ω and 950 µFD).

Triple transfections containing mCh-Drp1, Mito-BFP (Addgene, plasmid #49151) and Dyn2-GFP (gift from Gia Voeltz) were performed with Lipofectamine 2000. Such transfections were carried out in using 80 ng of mCh-Drp1, 100 ng of Dyn2-GFP and 80 ng of Mito-BFP and 1.5 µL of Lipofectamine 2000. Dual color imaging of dynamin was performed using double transfections of either 100 ng Dyn2-GFP and 150 ng Mito-Scarlet, or 100 ng Dyn2-mCherry and 150 ng Mito-GFP. Triple transfection containing Mito-BFP, Drp1-GFP and KDEL-RFP were performed with Lipofectamine 2000. Such transfections were performed using 100 ng Mito-BFP, 100 ng Drp1-GFP and 100 ng KDEL-RFP. All quantities listed are per well of cells containing 2 mL of culture medium and carried out with Opti-MEM. The Lipofectamine mixture sat for 20 min before its addition to cells.

Drug treatment.

Nocodazole was diluted to a stock solution of 10 mM in DMSO. To depolymerize microtubules, cells were incubated with 10µM Nocodazole (Sigma-Aldrich) for 1h before imaging (1 µL Nocodazole per 1000 µL

medium). Control cells were incubated with the equivalent volume of DMSO for 1h before imaging (1 µL DMSO per 1000 µL medium).

SIM imaging and reconstruction.

Fast dual-color SIM imaging was performed at Janelia Farm with an inverted fluorescence microscope (AxioObserver; Zeiss) using an SLM (SXGA-3DM; Fourth Dimension Displays) to create the illumination pattern and liquid crystal cell (SWIFT; Meadowlark) to control the polarization. Fluorescence was collected through a 100X 1.49 NA oil immersion objective and imaged onto a digital CMOS camera (ORCA-Flash4.0 v2 C11440; Hamamatsu). Time-lapse images were acquired every 1 s for 3-5 min, with 50 ms exposure time. Fast dual color imaging of mitochondria and Drp1 was performed at 37˚C with 5% CO2, in pre-warmed DMEM medium. Dual-color SIM imaging for Nocodazole and Dyn2 experiments was performed on an inverted fluorescence microscope (Eclipse Ti; Nikon) equipped with an electron charge coupled device camera (iXon3 897; Andor Technologies). Fluorescence was collected with through a 100x 1.49 NA oil immersion objective (CFI Apochromat TIRF 100XC Oil; Nikon). Images were captured using NIS elements with SIM (Nikon) resulting in temporal resolution of 1 s for single-color and 6-8s for dual-color imaging, with 50 ms exposure time. Imaging was performed at 37˚C in pre-warmed Leibovitz medium. See SI for details on iSIM imaging, image reconstruction and analysis.

SIM images were reconstructed using a custom 2D linear SIM reconstruction software obtained at Janelia farm, as previously described [58, 59]. Images were reconstructed using a generalized Weiner filter parameter value of 0.02-0.05 with background levels of ~100.

iSIM imaging and reconstruction.

For iSIM experiments, imaging was performed on a custom-built microscope setup as previously described [60, 61]. The microscope was equipped with a 1.49 NA oil immersion objective (APONXOTIRF; Olympus), with 488 nm and 561 nm excitation lasers and an sCMOS camera (Zyla 4.2; Andor). Images were captured at 0.1-0.3 s temporal resolution for both channels. All imaging was performed at 37˚C in

pre-warmed Leibovitz medium. Raw iSIM images were deconvolved using the Lucy-Richardson deconvolution algorithm [62, 63] implemented in MATLAB, run for 40 iterations.

Confocal imaging.

Confocal imaging was performed on an inverted microscope (DMI 6000; Leica) equipped with hybrid photon counting detectors (HyD; Leica). Fluorescence was collected through a 63x 1.40 NA oil immersion objective (HC PL APO 63x/1.40 Oil CS2; Leica). Images were captured using the LAS X software (Leica). All imaging was performed at 37˚C in pre-warmed Leibovitz medium.

STORM imaging and reconstruction.

For STORM imaging, prior to staining, cells were washed with PBS (Sigma). Cells were incubated with MitoTracker Red CMXRos (LifeTechnologies) at a concentration of 500 nM for 5 minutes, before washing again with PBS.

For measuring mitochondrial membrane potential, cells were incubated with 100 nM TMRE (Abcam, ab113852) for 10 minutes before time-lapse measurements.

STORM imaging was performed at room temperature in a glucose-oxidase/catalase (Glox) oxygen removal buffer described in Shim et al [30]. Briefly, a 2% glucose solution is prepared in DMEM (Gibco). Glucose oxidase (0.5 mg/mL) and catalase (40 µg/mL) were added to the glucose solution and the pH was left to drop for 30-60 min. After this time, the pH was adjusted to 7 yielding a final solution with 6.7% HEPES. Imaging was performed on an inverted microscope (IX71; Olympus) equipped with a 100x NA 1.4 oil immersion objective (UPlanSAPO100X; Olympus) using an electron multiplying CCD camera (iXon+; Andor Technologies), with a resulting pixel size of 100nm. Laser intensities were between 1-5 $kWcm^{-2}$.

For STORM datasets, single molecules were localized using the RapidSTORM v3.3 software [64]. Local signal-to-noise detection with a threshold value of 50 was used. Peaks with a width between 70-300 nm and at least 200 photons were rendered for the final STORM image.

FliptR synthesis.

The FliptR probe was synthesized following previously reported procedures [45]. For mitochondrial targeting, compounds 2,3 and 5 were synthesized and purified according to procedures that will be reported elsewhere in another manuscript [46] in due time (SFig. 7).

Compound 5 was synthesized and purified according to procedures described in [46] (SFig. 7).

The probe can report on membrane tension as reported in reference [45]. Spectroscopic characterizations, mechanosensitive behavior in LUVs and GUVs of various lipid composition, colocalization studies in mitochondria and response of fluorescence lifetime to osmotic shocks (i.e. membrane tension changes) will be reported elsewhere in another manuscript [46] in due time.

FLIM imaging and analysis.

For FLIM imaging with the mitochondria-targeted FliptR probe, cells were incubated with 500 nM of the probe solution for 15 min, and washed before imaging. Imaging was performed using a Nikon Eclipse TI A1R microscope equipped with a time-correlated single-photon counting module from PicoQuant. A pulsed 485 nm laser (PicoQuant LDH-D-C-485) was used for excitation, operated at 20 MHz. The emission was collected through ha 600/50 nm bandpass filter, on a gated PMA hybrid 40 detector and a PicoHarp 300 board (PicoQuant).

FLIM data was analyzed using the SymPhoTime 64 software (PicoQuant). The fluorescence decay data was fit to a double exponential model after deconvolution for the calculated impulse response function. The values reported in the main text are the average lifetime intensity.

Statistics.

Statistics were performed using Matlab and OriginPro software. All datasets were tested for normal distribution using the D'Agostino-Pearson normality test (significance value of 0.05) [65]. If the datasets passed the test, then statistical significance was determined using a two-tailed t-tests. If datasets failed the normality test, a nonparametric test was chosen to compare the significance of means between groups

Mann-Whitney test for two samples (with one or two tailed distributions where appropriate) and Kruskal-Wallis ANOVA for multiple samples [66]. $P<0.05$ were considered as significant and were marked by '*'; $P<0.01$ with '**', $P<0.001$ by '***' and $P<0.0001$ by '****'.

Curve fitting was performed using the curve fitting toolbox in Matlab.